Research Square

Preprints are preliminary reports that have not undergone peer review.
They should not be considered conclusive, used to inform clinical practice,
or referenced by the media as validated information.

# Gravitational-Wave Echoes from a Hayward Black Hole under Minimal Geometric Deformation

**Owais Farooq Dar**

owai24831@outlook.com

Canadian Quantum Research Center

**Research Article**

**Keywords:** regular black holes, gravitational perturbations, minimal geometric deformation, Hayward black hole, gravitational-wave echoes

**Posted Date:** July 13th, 2026

**DOI:** https://doi.org/10.21203/rs.3.rs-9459322/v1

**License:** This work is licensed under a Creative Commons Attribution 4.0 International License.
Read Full License

**Additional Declarations:** No competing interests reported.

# Gravitational-Wave Echoes from a Hayward Black Hole under Minimal Geometric Deformation

Owais Farooq[1,2*]

[1*]Department of Physics, Central University of Kashmir, Tulmulla , Ganderbal (191131), India.
[2*]Canadian Quantum Research Center (CQRC), 460 Doyle Ave, Unit 106, Kelowna, BC, Canada..

Corresponding author(s). E-mail(s): owai24831@outlook,com;

**Abstract**

We study a regular black-hole geometry obtained by applying a radial minimal geometric deformation (MGD) of dimensionless strength $\boldsymbol{\alpha}$ to the Hayward seed, characterized by its ADM mass $\boldsymbol{M}$ and its regularity scale $\boldsymbol{g}$,and then trace the construction through the odd-parity perturbation problem. The background sector is kept exact: the deformation function is written in closed form, the Einstein equations separate into seed and decoupler blocks (the decoupler being the additional effective source that deforms the seed), asymptotic flatness is preserved, and the deformed metric remains curvature regular at the center while inheriting the seed horizon structure in an explicit admissible range of the deformation parameter $\boldsymbol{\alpha}$. In the axial sector we work under the frozen-source odd-parity closure appropriate to a static anisotropic background without an independent propagating odd matter mode. Within that framework the master equation acquires an exact effective potential whose seed contribution retains the nonvacuum Hayward correction proportional to the radial derivative $\boldsymbol{m'_H(r)}$ of the Hayward mass function $\boldsymbol{m_H(r)}$ and whose decoupling contribution is isolated analytically. We show that this potential passes from a single-barrier profile to a genuine max–min–max structure in an open region of the $\boldsymbol{(g, \alpha)}$ plane, so the exact geometry itself supplies a trapping cavity without any externally imposed mirror or phenomenological reflecting surface. A representative characteristic evolution is then used to connect the potential structure to delayed secondary pulses in the time domain. The analysis makes each algebraic step explicit, states every assumption at the point of use, distinguishes exact statements from numerical evidence, and records the numerical methodology in enough detail for direct audit and reproduction.

**Keywords:** regular black holes, gravitational perturbations, minimal geometric deformation, Hayward black hole, gravitational-wave echoes

# Contents

**1 Introduction** **2**

**2 Exact decoupled regular background** **5**

**3 Axial perturbations, trapping structure, and phase map** **12**

**4 Time-domain signal and echo scale** **19**

**5 Discussion** **21**

**A Field equations for the static spherical ansatz** **30**

**B Expanded near-center curvature analysis** **31**

**C Odd-parity reduction and phase-map criterion** **32**

**D Characteristic evolution, convergence, robustness, and sampled data** **33**

# 1 Introduction

Regular black holes remain among the clearest effective settings in which one can ask how interior singular behavior may be softened while the exterior horizon structure remains accessible to classical analysis. The singularity theorems of Penrose and of Hawking and Penrose place geodesic incompleteness at the end of gravitational collapse once focusing, trapped surfaces, and global causal conditions are combined [1–3]. In the black-hole problem this leaves the exterior domain highly constrained and pushes the interior toward a regime where the classical description is expected to require completion. Regular geometries were introduced precisely to reorganize that interior regime. Bardeen, Dymnikova, Ayón-Beato and García, Bronnikov, and Hayward gave explicit models in which the central curvature divergence is replaced by finite invariants while horizon structure can still survive [4–9]. Reviews and recent developments have kept that program active, both as an effective description of singularity softening and as a target for observational discrimination [10–18].

A second strand of work concerns compact objects supported by anisotropic stresses, additional matter sectors, or effective gravitational sources. Minimal geometric deformation (hereafter MGD) provides a particularly transparent language for that setting because it starts from a known seed solution and deforms one metric sector while preserving a clean separation between the seed stress tensor and the additional source sector [20–26]. Throughout the paper we follow the standard terminology of the gravitational-decoupling literature: the known solution used as the starting point is

called the *seed*, and the additional effective source $\Theta_{\mu\nu}$ that deforms the seed is called the *decoupler*, because the Einstein equations separate (decouple) into a seed block and a block sourced purely by $\Theta_{\mu\nu}$.The same framework has produced compact-star models, hairy black holes, and regular black holes built directly in the decoupling language [27, 28]. In the present problem that formalism offers an exact way of separating two physical ingredients that are often intertwined in more phenomenological constructions: the short-distance regularity scale encoded by the seed mass profile and the anisotropic reshaping induced by the decoupler.

The perturbative motivation comes from black-hole spectroscopy. The Regge–Wheeler and Zerilli analyses, the scattering picture of Vishveshwara, the frequency-domain methods of Leaver, Schutz and Will, Iyer and Will, Nollert, Kokkotas and Schmidt, and later reviews by Berti, Cardoso, Starinets, Konoplya, Zhidenko, and others established quasinormal ringing as a direct probe of exterior geometry [30–44]. In the observational era inaugurated by the first LIGO/Virgo detections, late-time ringdown and related secondary structures acquired a direct phenomenological role [45, 47, 48]. Echo-like delayed pulses are especially interesting in that context. A broad literature studies them through partially reflecting near-horizon structures, thin shells, exotic compact objects, or multibarrier potentials [49–56]. The present paper focuses on the geometric mechanism alone: if the exact axial potential of a black-hole background develops two exterior barriers separated by a local minimum, temporary trapping supplies a natural route to delayed pulses.

This manuscript studies that mechanism in a corner that differs from the recent decoupling-based echo literature in one important respect. The seed geometry is already regular before the decoupler is activated. The deformation is kept analytic throughout, so the background remains exact rather than semi-phenomenological. The main question is therefore sharp: can the combination of a regular Hayward core and a radial minimal geometric deformation reorganize the exact axial potential strongly enough to create an exterior trapping cavity? The central result is that, within the frozen-source odd-parity closure used in the axial sector, the answer is yes. The regularity scale and the decoupling profile enter the effective potential in analytically separable pieces, and their combined action produces an open region of parameter space with a max–min–max profile. The associated delayed signal then appears in a representative characteristic evolution without the need for an externally prescribed mirror.

It is useful to state explicitly how this paper sits relative to the closest neighboring literature. The Hayward perturbation analysis of Malik [58] focuses on the perturbative properties of the Hayward spacetime itself, whereas the present work starts from the Hayward seed and then deforms the radial sector through an exact MGD profile before deriving the odd-parity potential of the resulting background. The recent decoupling-based echo analysis of Yang *et al.* [29] studies echo-like signals in a hairy black hole generated within gravitational decoupling. The present paper differs in that the seed geometry is already regular prior to decoupling, the background deformation is kept in closed form throughout, and the axial potential is decomposed so that the nonvacuum Hayward contribution and the decoupling contribution can be read off separately. The

novelty therefore lies in the exact regular-seed-plus-deformation mechanism itself rather than in a generic statement that multibarrier behavior may occur in decoupled systems.

The paper is organized around four technical objectives. First, every load-bearing formula is either derived directly or tied to a standard reduction with an explicit citation and an explicit statement of assumptions. Second, the background construction is written so that horizon inheritance, asymptotic flatness, near-center regularity, and the status of the reconstructed decoupler closure can be audited step by step. Third, the odd-parity sector is presented in a way that makes the nonvacuum seed contribution and the decoupling correction fully transparent. Fourth, the numerical part is stated as a reproducible procedure with an explicit phase-map criterion, a precise pulse-identification rule, and a clear distinction between exact statements and representative numerical evidence.

What is established exactly in the present paper is the existence of the deformed background, the separated Einstein-system structure, the horizon-inheritance condition, the finiteness of the curvature invariants at the center, the exact form of the axial potential under the stated closure, and the existence of a cavity-producing open region around a representative point. What is shown numerically is the location of the cavity region in the $(g, \alpha)$ plane, the evolution of the critical radii and barrier depths, and a representative delayed-pulse pattern in the time domain. What is interpreted physically is the connection between the deformed potential and temporary trapping of odd-parity radiation. What remains outside the present scope is a full quasinormal-mode survey, a polar-sector analysis, and an observational inference study based on the phase map. The restriction to the axial sector is deliberate rather than incidental. In the odd-parity channel a static, diagonal, parity-even effective source admits the frozen-source closure used here: the matter sector carries no independent odd-parity dynamical variable, so the perturbation problem closes on the metric alone and reduces to a single exact master equation. No analogous closure is available in the polar sector, because even-parity metric perturbations couple directly to perturbations of the effective density and pressures through the constraint equations, so a polar analysis would require an explicit dynamical model for the decoupler fluctuations rather than only its background profile. That model dependence, and the associated coupled system replacing the single Schrödinger-type equation, is the bottleneck we anticipate for the polar extension; it is discussed further in Section 5.

The paper is organized as follows. Section II develops the exact deformed background, derives the separated Einstein equations, reconstructs the decoupler closure from the chosen deformation profile, and proves curvature regularity. Section III studies the odd-parity sector, states the closure assumption precisely, derives the exact potential decomposition, and identifies the trapping region. Section IV derives the characteristic evolution scheme and relates the time-domain signal to the exact tortoise geometry. Section V summarizes the status of the results and the natural next technical steps. Appendix A gives the field-equation derivation for the static spherical ansatz. Appendix B records the near-center curvature analysis in expanded form. Appendix C documents the odd-parity reduction used in the axial sector and the classification criterion behind the phase map. Appendix D gives the numerical evolution details, convergence tests, robustness checks, geometric delay comparison, and sampled waveform data.

## 2 Exact decoupled regular background

We begin with the static, spherically symmetric line element

$$ds^2 = -A(r)\,dt^2 + \frac{dr^2}{B(r)} + r^2\left(d\theta^2 + \sin^2\theta\,d\phi^2\right), \tag{2.1}$$

with $A(r) > 0$ and $B(r) > 0$ in the exterior static region. For later use we record the nonvanishing diagonal metric components and their inverses:

$$g_{tt} = -A(r), \qquad g_{rr} = \frac{1}{B(r)}, \qquad g^{tt} = -\frac{1}{A(r)}, \qquad g^{rr} = B(r). \tag{2.2}$$

The nonvanishing Christoffel symbols are listed in Appendix A. A direct substitution into the Einstein tensor gives the independent field equations

$$8\pi\rho^{\rm eff} = \frac{1-B}{r^2} - \frac{B'}{r}, \tag{2.3}$$

$$8\pi p_r^{\rm eff} = -\frac{1-B}{r^2} + \frac{B}{r}\frac{A'}{A}, \tag{2.4}$$

$$8\pi p_t^{\rm eff} = \frac{B}{2}\frac{A''}{A} - \frac{B}{4}\left(\frac{A'}{A}\right)^2 + \frac{B'}{4}\frac{A'}{A} + \frac{B}{2r}\frac{A'}{A} + \frac{B'}{2r}, \tag{2.5}$$

while covariant conservation of the effective source takes the form

$$\left(p_r^{\rm eff}\right)' + \frac{A'}{2A}\left(\rho^{\rm eff} + p_r^{\rm eff}\right) + \frac{2}{r}\left(p_r^{\rm eff} - p_t^{\rm eff}\right) = 0. \tag{2.6}$$

Throughout we use the convention $G_{\mu\nu} = 8\pi T_{\mu\nu}$ and the effective stress tensor $T^{\mu}{}_{\nu} = \mathrm{diag}[-\rho, p_r, p_t, p_t]$.

The seed geometry is the Hayward metric,

$$A(r) = B(r) = \mu(r), \qquad \mu(r) = 1 - \frac{2Mr^2}{r^3 + 2Mg^2} = 1 - \frac{2m_H(r)}{r}, \tag{2.7}$$

with effective mass function

$$m_H(r) = \frac{Mr^3}{r^3 + 2Mg^2}. \tag{2.8}$$

Here $M$ is the ADM mass and $g$ is the regularity scale. The horizon condition $\mu(r_H) = 0$ is equivalent to

$$r_H^3 - 2Mr_H^2 + 2Mg^2 = 0. \tag{2.9}$$

The extremal point is obtained by imposing a double root. Differentiation of (2.7) gives

$$\mu'(r) = \frac{2Mr\left(r^3 - 4Mg^2\right)}{\left(r^3 + 2Mg^2\right)^2}. \tag{2.10}$$

At extremality one has simultaneously $\mu(r_H) = 0$ and $\mu'(r_H) = 0$, so $r_H^3 = 4Mg^2$ and $r_H = 4M/3$. Substituting into (2.9) yields

$$g_{\rm ext}^2 = \frac{16M^2}{27}. \tag{2.11}$$

Hence the seed has two horizons for $g^2 < 16M^2/27$, a degenerate horizon at the threshold, and no horizon above that value [9–11].

The total source is decomposed into the Hayward sector and an additional decoupler sector,

$$G_{\mu\nu} = 8\pi \left( T_{\mu\nu}^{(H)} + \alpha\, \Theta_{\mu\nu} \right) \equiv 8\pi T_{\mu\nu}^{\rm eff}, \tag{2.12}$$

where $\alpha$ is the dimensionless deformation parameter. In the radial minimal geometric deformation prescription one keeps the temporal metric function fixed and deforms only the radial sector,

$$A(r) = \mu(r), \qquad B(r) = \mu(r) + \alpha f(r). \tag{2.13}$$

Inserting (2.13) into (2.3)–(2.5) and collecting the terms that carry no factor of $\alpha$ gives the seed system

$$8\pi\rho_H = \frac{1-\mu}{r^2} - \frac{\mu'}{r}, \tag{2.14}$$

$$8\pi p_{rH} = -\frac{1-\mu}{r^2} + \frac{\mu'}{r}, \tag{2.15}$$

$$8\pi p_{tH} = \frac{\mu''}{2} + \frac{\mu'}{r}. \tag{2.16}$$

The remaining terms are linear in $f$ and define the decoupler block,

$$8\pi\rho_\theta = \frac{f'}{r} + \frac{f}{r^2}, \tag{2.17}$$

$$8\pi p_{r\theta} = \frac{f}{r}\frac{\mu'}{\mu} + \frac{f}{r^2}, \tag{2.18}$$

$$8\pi p_{t\theta} = \frac{f}{2}\frac{\mu''}{\mu} - \frac{f}{4}\left(\frac{\mu'}{\mu}\right)^2 + \frac{f'}{4}\frac{\mu'}{\mu} + \frac{f}{2r}\frac{\mu'}{\mu} + \frac{f'}{2r}. \tag{2.19}$$

The decomposition is exact for the radial MGD ansatz because the Einstein equations are affine in $B$ and $B'$ when $A$ is kept fixed.

The Hayward sector can be written explicitly by differentiating (2.7). Since

$$1 - \mu(r) = \frac{2Mr^2}{r^3 + 2Mg^2}, \qquad \frac{\mu'(r)}{r} = \frac{2M\left(r^3 - 4Mg^2\right)}{\left(r^3 + 2Mg^2\right)^2}, \tag{2.20}$$

one finds

$$8\pi\rho_H = \frac{2M}{r^3+2Mg^2} - \frac{2M\left(r^3-4Mg^2\right)}{\left(r^3+2Mg^2\right)^2} = \frac{12M^2g^2}{\left(r^3+2Mg^2\right)^2}, \tag{2.21}$$

$$8\pi p_{rH} = -\frac{2M}{r^3+2Mg^2} + \frac{2M\left(r^3-4Mg^2\right)}{\left(r^3+2Mg^2\right)^2} = -\frac{12M^2g^2}{\left(r^3+2Mg^2\right)^2}. \tag{2.22}$$

Thus

$$\rho_H = \frac{3M^2g^2}{2\pi\left(r^3+2Mg^2\right)^2}, \qquad p_{rH} = -\rho_H. \tag{2.23}$$

For the tangential pressure one differentiates (2.10) once more. The result can be written as

$$\mu''(r) = \frac{4M\left(-r^6+14Mg^2r^3-4M^2g^4\right)}{\left(r^3+2Mg^2\right)^3}, \tag{2.24}$$

and substitution into (2.16) gives

$$p_{tH} = \frac{3M^2g^2\left(r^3-Mg^2\right)}{\pi\left(r^3+2Mg^2\right)^3}. \tag{2.25}$$

These expressions show that the Hayward seed is anisotropic and nonvacuum away from the center. That point matters later because the seed axial potential contains an explicit matter correction.

The next step is to choose a deformation profile that is analytically manageable, decays at large radius, and stays regular at the center. In the present construction the decoupler closure is reconstructed from a chosen $f(r)$ rather than postulated independently. Before displaying the profile it is worth stating the motivation for both choices made in this section, since neither is arbitrary. The Hayward metric is adopted as the seed because it is the minimal one-scale regular black hole: a single parameter $g$ controls the departure from Schwarzschild, the horizon structure is known in closed form through the cubic (2.9), the source is a simple anisotropic effective fluid, and the geometry has become a standard benchmark in the regular-black-hole and perturbation literature [9, 10, 57, 58], which makes the effect of the deformation easy to isolate and compare. The deformation profile is then selected by four structural requirements rather than by phenomenological fitting: (i) it must be proportional to the seed function $\mu(r)$, so that the zeros of $B(r)$ coincide with the zeros of $\mu(r)$ and the seed horizons are inherited exactly; (ii) it must vanish quadratically at the center, so that the near-center expansion and the curvature invariants remain finite; (iii) it must decay at least as fast as $r^{-2}$ at large radius, so that asymptotic flatness and the ADM mass of the seed are preserved; and (iv) it should be tied to the regularity scale itself, which is achieved through the overall factor $g^2$ and the denominator $(r^2+g^2)^3$, so that the deformation switches off in the singular limit $g \to 0$ and the construction probes precisely the interplay between regularity and decoupling. The factor $(r-2M)^2$ keeps the profile nonnegative while suppressing it near the Schwarzschild-scale radius, which localizes the deformation in the exterior region where the potential reshaping

takes place. We take

$$f(r) = 16\,\mu(r)\,\frac{g^2 r^2 (r-2M)^2}{(r^2+g^2)^3}. \tag{2.26}$$

We emphasize that no claim is made that the deformed spacetime is more physical than the Hayward seed itself. The deformed family should be read as a controlled, exact one-parameter environment for the regular seed: it is the simplest closed-form setting in which one can ask how an anisotropic decoupling sector reshapes the exterior perturbative structure of an already regular geometry, while every admissibility, regularity, and asymptotic property remains auditable analytically. It is convenient to factor out the seed function and define

$$\Xi(r) = 16\,\frac{g^2 r^2 (r-2M)^2}{(r^2+g^2)^3}, \qquad B(r) = \mu(r)\,[1+\alpha\Xi(r)]\,. \tag{2.27}$$

The function $\Xi(r)$ is continuous on $[0,\infty)$, satisfies $\Xi(0)=0$, $\Xi(2M)=0$, and obeys $\Xi(r)\to 0$ as $r\to\infty$. It therefore attains a finite global maximum on $[0,\infty)$. Since every factor in (2.27) is nonnegative, one has

$$\Xi(r) \geq 0 \quad \text{for all } r \geq 0. \tag{2.28}$$

A direct large-$r$ expansion gives

$$\Xi(r) = \frac{16g^2}{r^2} - \frac{64Mg^2}{r^3} + \mathcal{O}(r^{-4}), \tag{2.29}$$

so asymptotic flatness is preserved because

$$B(r) = 1 - \frac{2M}{r} + \frac{16\alpha g^2}{r^2} + \mathcal{O}(r^{-3}). \tag{2.30}$$

The admissibility condition for horizon inheritance is then

$$1+\alpha\Xi(r) > 0 \quad \text{for all } r \geq 0. \tag{2.31}$$

A sufficient and convenient way of stating it is

$$\alpha > -\frac{1}{\Xi_{\max}}, \qquad \Xi_{\max} = \max_{r\geq 0}\Xi(r). \tag{2.32}$$

Under (2.32) the sign of $B(r)$ is the sign of $\mu(r)$ at every radius. The zeros of $B$ therefore coincide with the zeros of the seed function, and the seed horizons are inherited without shifting their positions.

Because the decoupler closure is reconstructed from the chosen deformation profile, it is useful to display that reconstruction explicitly. Suppose that the decoupler radial pressure and density satisfy a local ratio

$$p_{r\theta}(r) = w(r)\,\rho_\theta(r). \tag{2.33}$$

Using (2.17) and (2.18) one obtains

$$\frac{\mu'}{\mu} + \frac{1}{r} = w(r)\left(\frac{f'}{f} + \frac{1}{r}\right). \tag{2.34}$$

Now take the logarithm of (2.26),

$$\ln f = \ln 16 + \ln g^2 + \ln \mu + 2\ln r + 2\ln(r-2M) - 3\ln(r^2+g^2), \tag{2.35}$$

and differentiate:

$$\frac{f'}{f} = \frac{\mu'}{\mu} + \frac{2}{r} + \frac{2}{r-2M} - \frac{6r}{r^2+g^2}. \tag{2.36}$$

Substituting (2.36) into (2.34) and solving for $w(r)$ gives

$$w(r) = \frac{r\mu'/\mu + 1}{r\mu'/\mu + 3 + \dfrac{2r}{r-2M} - \dfrac{6r^2}{r^2+g^2}}. \tag{2.37}$$

The point of this formula is interpretive rather than dynamical. The stress tensor is determined by $f(r)$ through (2.17)–(2.19); the ratio $w(r)$ is an auxiliary diagnostic reconstructed from that exact choice. Since $f(r)$ contains the factor $(r-2M)^2$, the decoupler density changes sign at $r = 2M$, and the denominator of (2.37) vanishes linearly there. The resulting simple pole in $w(r)$ is therefore a feature of the ratio representation rather than a singularity of the stress tensor itself.

The exact deformed geometry is thus

$$g_{tt} = -\mu(r), \qquad g_{rr} = \frac{1}{\mu(r)\,[1+\alpha\Xi(r)]}. \tag{2.38}$$

The regularity analysis is most transparent near the center. Using

$$\frac{2Mr^2}{r^3+2Mg^2} = \frac{r^2}{g^2}\left(1 + \frac{r^3}{2Mg^2}\right)^{-1} = \frac{r^2}{g^2} - \frac{r^5}{2Mg^4} + \mathcal{O}(r^8), \tag{2.39}$$

one finds

$$A(r) = \mu(r) = 1 - \frac{r^2}{g^2} + \frac{r^5}{2Mg^4} + \mathcal{O}(r^8). \tag{2.40}$$

For the deformation factor,

$$(r-2M)^2 = 4M^2 - 4Mr + r^2, \qquad (r^2+g^2)^3 = g^6\left(1 + \frac{r^2}{g^2}\right)^3, \tag{2.41}$$

so

$$\Xi(r) = \frac{64M^2}{g^4}r^2 - \frac{64M}{g^4}r^3 + \mathcal{O}(r^4), \tag{2.42}$$

and therefore

$$B(r) = 1 + \left(-\frac{1}{g^2} + \frac{64\alpha M^2}{g^4}\right) r^2 - \frac{64\alpha M}{g^4} r^3 + \mathcal{O}(r^4). \tag{2.43}$$

This shows two things immediately. First, the metric functions remain finite at the center. Second, the leading even-order terms in $A$ and $B$ coincide only when $\alpha = 0$, so the deformed center remains curvature regular without coinciding with an exact de Sitter core in the strict sense.

To make the curvature statement explicit, introduce the orthonormal frame associated with (2.1). The independent orthonormal Riemann components are

$$R_{\hat{t}\hat{r}\hat{t}\hat{r}} = -\frac{B}{2}\nu'' - \frac{B}{4}\nu'^2 - \frac{B'}{4}\nu', \tag{2.44}$$

$$R_{\hat{t}\hat{\theta}\hat{t}\hat{\theta}} = -\frac{B\nu'}{2r}, \tag{2.45}$$

$$R_{\hat{r}\hat{\theta}\hat{r}\hat{\theta}} = -\frac{B'}{2r}, \tag{2.46}$$

$$R_{\hat{\theta}\hat{\phi}\hat{\theta}\hat{\phi}} = \frac{1-B}{r^2}, \tag{2.47}$$

where $\nu = \ln A$. The Kretschmann scalar is

$$K = 4\left(R_{\hat{t}\hat{r}\hat{t}\hat{r}}\right)^2 + 8\left(R_{\hat{t}\hat{\theta}\hat{t}\hat{\theta}}\right)^2 + 8\left(R_{\hat{r}\hat{\theta}\hat{r}\hat{\theta}}\right)^2 + 4\left(R_{\hat{\theta}\hat{\phi}\hat{\theta}\hat{\phi}}\right)^2. \tag{2.48}$$

Now write

$$A(r) = 1 + a_2 r^2 + \mathcal{O}(r^5), \qquad B(r) = 1 + b_2 r^2 + b_3 r^3 + \mathcal{O}(r^4), \tag{2.49}$$

with

$$a_2 = -\frac{1}{g^2}, \qquad b_2 = -\frac{1}{g^2} + \frac{64\alpha M^2}{g^4}. \tag{2.50}$$

Then

$$\nu(r) = a_2 r^2 + \mathcal{O}(r^5), \qquad \nu'(r) = 2a_2 r + \mathcal{O}(r^4), \qquad \nu''(r) = 2a_2 + \mathcal{O}(r^3), \tag{2.51}$$

and

$$B'(r) = 2b_2 r + \mathcal{O}(r^2). \tag{2.52}$$

Substituting into (2.44)–(2.48) yields

$$R_{\hat{t}\hat{r}\hat{t}\hat{r}} = -a_2 + \mathcal{O}(r), \qquad R_{\hat{t}\hat{\theta}\hat{t}\hat{\theta}} = -a_2 + \mathcal{O}(r), \qquad R_{\hat{r}\hat{\theta}\hat{r}\hat{\theta}} = -b_2 + \mathcal{O}(r), \qquad R_{\hat{\theta}\hat{\phi}\hat{\theta}\hat{\phi}} = -b_2 + \mathcal{O}(r), \tag{2.53}$$

and therefore

$$K(r) = 12\left(a_2^2 + b_2^2\right) + \mathcal{O}(r). \tag{2.54}$$

The finite central limit is

$$K(0) = \frac{12}{g^8}\left[g^4 + \left(g^2 - 64\alpha M^2\right)^2\right]. \tag{2.55}$$

The same expansion structure also guarantees the finiteness of the Ricci scalar and $R_{\mu\nu}R^{\mu\nu}$. The geometry is therefore curvature regular at the center. What is established here is finiteness of the invariants and of the orthonormal Riemann components. The deformed metric does not satisfy the stronger statement of an exact de Sitter core once the odd cubic term in (2.43) is present.

Figure 1 summarizes the background sector. The upper panels show the seed lapse function and the deformation profile. The lower-left panel shows how the exterior radial metric function changes with $\alpha$ while the horizon positions remain inherited in the admissible region. The lower-right panel shows the finite central Kretschmann scalar as a function of the deformation parameter.

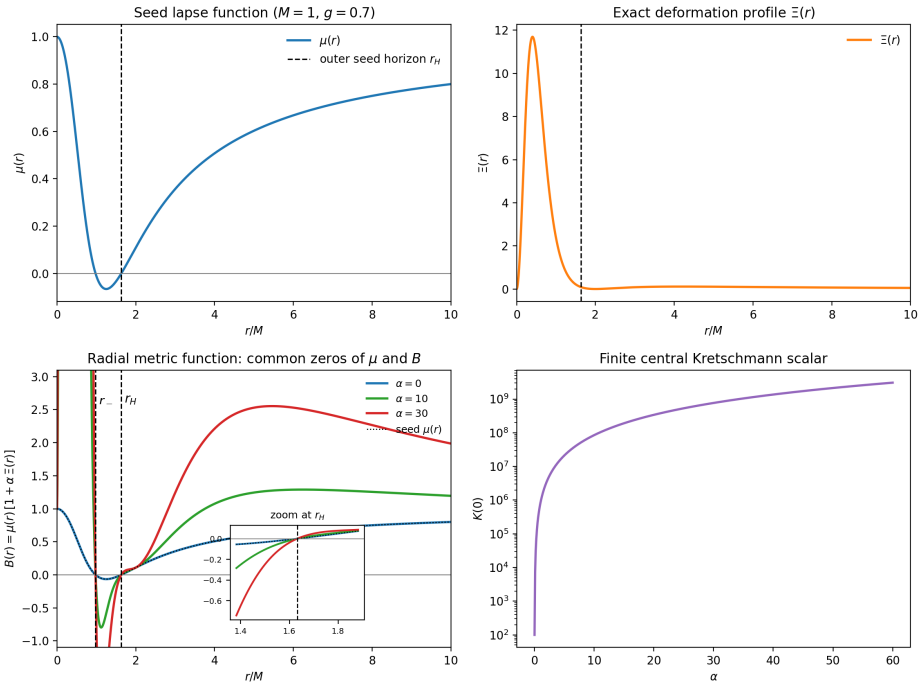



**Fig. 1** Background properties of the deformed Hayward geometry. The upper-left panel shows the seed lapse function $\mu(r)$ for $M = 1$ and $g = 0.7$, together with the outer seed horizon. The upper-right panel shows the exact deformation profile $\Xi(r)$ defined in (2.27). The lower-left panel shows the radial metric function $B(r) = \mu(r)[1 + \alpha\Xi(r)]$ for $\alpha = 0, 10, 30$ over the full radial range, together with the seed lapse $\mu(r)$ (dotted). The panel now displays explicitly that all curves vanish at the same two radii, the inner and outer seed horizons $r_- \simeq 0.980$ and $r_H \simeq 1.632$ (dashed vertical lines), with the inset zooming in on the common zero crossing at $r_H$; this demonstrates directly that the zeros of $B$ coincide with those of the seed lapse $\mu$ shown in the upper-left panel whenever (2.32) holds. The lower-right panel plots the finite central Kretschmann scalar (2.55) versus $\alpha$ on logarithmic scale and therefore visualizes the curvature-regular character of the deformed center.

# 3 Axial perturbations, trapping structure, and phase map

We now turn to the odd-parity sector. The analysis in this section uses one explicit assumption that must be stated sharply because it is load-bearing. Throughout, by a *closure* we mean the set of assumptions that closes the linearized field equations into a well-posed system for a definite set of variables; different closures correspond to different physical assumptions about which perturbative degrees of freedom are dynamical. We adopt the frozen-source odd-parity closure appropriate to a static anisotropic background with no independent propagating odd-parity matter degree of freedom. Operationally this means that the odd-parity metric perturbation evolves on the fixed background and the matter sector contributes only through the background

functions $A(r)$ and $B(r)$. This is the same closure used in standard axial perturbation analyses of static fluid or anisotropic backgrounds when the source sector carries no separate axial dynamical variable [33]. Within that framework the perturbation problem reduces to a single Schrödinger-type equation. The present paper keeps that closure fixed throughout and makes no claim about the polar sector or about extensions with an independent odd matter mode.

The reason this closure is a consistent working assumption for the present model is structural. The background source is static, diagonal, and purely even under parity, and the radial MGD ansatz introduces no background axial current or off-diagonal angular-momentum flux. In a general matter-supported geometry the odd sector would couple to any independent axial perturbation of the source. Here the source is treated as an effective anisotropic medium specified completely by the background functions that solve the Einstein system, so the odd-parity dynamics is carried entirely by the metric once one assumes that the effective decoupler carries no separate propagating axial variable. In practical terms the working rule is that the odd-parity perturbation of the effective source is set to zero, while the full influence of that source is retained through the background coefficients $A(r)$ and $B(r)$. This is the precise scope of the axial calculation reported below.

In Regge–Wheeler gauge the axial metric perturbation is written as

$$h^{(\mathrm{ax})}_{\mu\nu}dx^\mu dx^\nu = -2h_0(t,r)\sin\theta\,\partial_\theta P_\ell(\cos\theta)\,dt\,d\phi - 2h_1(t,r)\sin\theta\,\partial_\theta P_\ell(\cos\theta)\,dr\,d\phi, \tag{3.1}$$

with $\ell \geq 2$. The angular dependence is fixed by

$$\frac{1}{\sin\theta}\partial_\theta\big(\sin\theta\,\partial_\theta P_\ell(\cos\theta)\big) = -\ell(\ell+1)P_\ell(\cos\theta). \tag{3.2}$$

Two remarks on the form of (3.1) are in order. First, in the general Regge–Wheeler gauge the odd-parity perturbation also contains $dt\,d\theta$ and $dr\,d\theta$ components, proportional to $\partial_\phi Y_{\ell m}/\sin\theta$; see, e.g., Ref. [44] for the full parametrization. Because the background is spherically symmetric, the perturbation equations are degenerate in the azimuthal number $m$, so we may set $m = 0$ without loss of generality. For $m = 0$ the spherical harmonics reduce to $P_\ell(\cos\theta)$ and the $\phi$-derivative vanishes identically, which is why the $dt\,d\theta$ and $dr\,d\theta$ terms are absent from (3.1). Second, the reduction summarized in (3.1)–(3.6) follows the standard odd-parity treatment of static spherically symmetric backgrounds [30, 32, 33, 38, 39], adapted to the anisotropic $A \neq B$ case in the notation of this paper. Under the frozen-source closure, the odd-parity Einstein system reduces to the usual pair of first-order equations for $h_0$ and $h_1$ on a static spherical background. Appendix C records the reduction used here and the field redefinition that removes the first radial derivative. After harmonic decomposition,

$$h_0(t,r) = e^{-i\omega t}H_0(r), \qquad h_1(t,r) = e^{-i\omega t}H_1(r), \tag{3.3}$$

one introduces

$$\Psi(r) = \frac{\sqrt{A(r)B(r)}}{r} H_1(r), \qquad \frac{dr_*}{dr} = \frac{1}{\sqrt{A(r)B(r)}}. \tag{3.4}$$

The axial sector then takes the Schrödinger form

$$\frac{d^2\Psi}{dr_*^2} + \left[\omega^2 - V_\ell(r)\right]\Psi = 0, \tag{3.5}$$

with effective potential

$$V_\ell(r) = A(r)\left[\frac{\ell(\ell+1)}{r^2} + \frac{2(B(r)-1)}{r^2}\right] - \frac{A(r)B'(r) + B(r)A'(r)}{2r}. \tag{3.6}$$

Equation (3.6) is the standard axial potential for a static spherical background in the present closure [30, 33, 38, 39] and is rederived in Appendix C in the notation of this paper, where the separation of the radial equations from the angular dependence is also outlined

For the deformed Hayward metric one has

$$A(r) = \mu(r), \qquad B(r) = \mu(r)\left[1 + \alpha\Xi(r)\right], \tag{3.7}$$

with

$$A'(r) = \mu'(r) = \frac{2Mr\left(r^3 - 4Mg^2\right)}{(r^3 + 2Mg^2)^2}, \qquad \frac{\Xi'(r)}{\Xi(r)} = \frac{2}{r} + \frac{2}{r-2M} - \frac{6r}{r^2+g^2}. \tag{3.8}$$

Substituting (3.7) into (3.6) and separating the terms according to their $\alpha$ dependence gives

$$\begin{aligned} V_\ell(r) = A(r)&\left[\frac{\ell(\ell+1)}{r^2} + \frac{2(A(r)-1)}{r^2} - \frac{A'(r)}{r}\right] \\ &+ \alpha A(r)\left[\frac{2A(r)\Xi(r)}{r^2} - \frac{A(r)\Xi'(r)}{2r} - \frac{A'(r)\Xi(r)}{r}\right]. \end{aligned} \tag{3.9}$$

This separation is exact. The first line depends only on the seed geometry and the second line is the pure decoupling correction,

$$V_\ell^{(1)}(r) = A(r)\left[\frac{2A(r)\Xi(r)}{r^2} - \frac{A(r)\Xi'(r)}{2r} - \frac{A'(r)\Xi(r)}{r}\right]. \tag{3.10}$$

The seed term deserves extra care because the Hayward metric is nonvacuum. Using

$$A(r) = 1 - \frac{2m_H(r)}{r}, \qquad A'(r) = -\frac{2m_H'(r)}{r} + \frac{2m_H(r)}{r^2}, \tag{3.11}$$

one finds

$$\frac{2(A-1)}{r^2} - \frac{A'}{r} = -\frac{4m_H}{r^3} - \frac{1}{r}\left(-\frac{2m'_H}{r} + \frac{2m_H}{r^2}\right)$$
$$= -\frac{6m_H}{r^3} + \frac{2m'_H}{r^2}. \tag{3.12}$$

Hence

$$V_\ell^{(0)}(r) = A(r)\left[\frac{\ell(\ell+1)}{r^2} - \frac{6m_H(r)}{r^3} + \frac{2m'_H(r)}{r^2}\right]. \tag{3.13}$$

For the Hayward mass profile,

$$m'_H(r) = \frac{6M^2g^2r^2}{(r^3+2Mg^2)^2}, \tag{3.14}$$

so the matter correction is finite and strictly positive for $r > 0$. The seed piece of the potential is therefore not obtained by inserting $m_H(r)$ into the vacuum Schwarzschild Regge–Wheeler expression and stopping there; the derivative term is an intrinsic consequence of the nonvacuum seed geometry.

The endpoint behavior follows directly from the metric functions. At a seed horizon $r_H$ one has $A(r_H) = 0$ and, under (2.32), $B(r_H) = 0$ as well, so

$$V_\ell(r_H) = 0. \tag{3.15}$$

At large radius,

$$A(r) = 1 - \frac{2M}{r} + \mathcal{O}(r^{-4}), \qquad \Xi(r) = \frac{16g^2}{r^2} + \mathcal{O}(r^{-3}), \tag{3.16}$$

and substitution into (3.9) gives

$$V_\ell(r) = \frac{\ell(\ell+1)}{r^2} - \frac{2M\left[\ell(\ell+1)+3\right]}{r^3} + \frac{32\alpha g^2}{r^4} + \mathcal{O}(r^{-5}). \tag{3.17}$$

Thus the exact potential vanishes at both ends of the exterior domain. Any change in barrier topology must therefore occur through interior creation or annihilation of critical points.

For the purposes of this paper a *genuine axial trapping cavity* means the following: in the exterior domain $r > r_H$ the exact potential possesses three distinct critical points

$$r_{\rm p}^{\rm in} < r_{\rm m} < r_{\rm p}^{\rm out}, \tag{3.18}$$

such that $r_{\rm p}^{\rm in}$ and $r_{\rm p}^{\rm out}$ are local maxima, $r_{\rm m}$ is a local minimum, and

$$V_\ell(r_{\rm p}^{\rm in}) > V_\ell(r_{\rm m}), \qquad V_\ell(r_{\rm p}^{\rm out}) > V_\ell(r_{\rm m}). \tag{3.19}$$

That criterion is implemented numerically by locating sign changes of $V'_\ell(r)$ on the exterior grid and then checking the height inequalities. Appendix C records the classification procedure used in the phase map.

A representative cavity-producing point is

$$M = 1, \qquad g = 0.7, \qquad \ell = 2, \qquad \alpha = 30. \tag{3.20}$$

The outer seed horizon obtained from (2.9) is

$$r_H \simeq 1.63212. \tag{3.21}$$

Direct evaluation of the exact derivative gives

$$V'_\ell(2.20) > 0, \qquad V'_\ell(2.24) < 0, \tag{3.22}$$

$$V'_\ell(2.38) < 0, \qquad V'_\ell(2.43) > 0, \tag{3.23}$$

$$V'_\ell(4.35) > 0, \qquad V'_\ell(4.40) < 0. \tag{3.24}$$

Since $V'_\ell(r)$ is continuous for $r > r_H$, the intermediate value theorem guarantees three distinct critical points with the bracketing intervals

$$r_{\rm p}^{\rm in} \in (2.20, 2.24), \qquad r_{\rm m} \in (2.38, 2.43), \qquad r_{\rm p}^{\rm out} \in (4.35, 4.40). \tag{3.25}$$

Numerically one finds

$$r_{\rm p}^{\rm in} \simeq 2.238, \qquad r_{\rm m} \simeq 2.404, \qquad r_{\rm p}^{\rm out} \simeq 4.356, \tag{3.26}$$

with

$$V_\ell(r_{\rm p}^{\rm in}) \simeq 0.10947, \qquad V_\ell(r_{\rm m}) \simeq 0.10884, \qquad V_\ell(r_{\rm p}^{\rm out}) \simeq 0.20130. \tag{3.27}$$

It is useful to state the corresponding barrier depths explicitly. Relative to the local minimum one has

$$\Delta V_{\rm in} = V_\ell(r_{\rm p}^{\rm in}) - V_\ell(r_{\rm m}) \simeq 6.3 \times 10^{-4}, \qquad \Delta V_{\rm out} = V_\ell(r_{\rm p}^{\rm out}) - V_\ell(r_{\rm m}) \simeq 9.246 \times 10^{-2}. \tag{3.28}$$

The onset cavity is therefore genuine and, at the same time, numerically delicate on the inner side. For that reason the classification is based on root isolation of $V'_\ell(r)$ and on the positive-height test (3.19), rather than on the visual appearance of a shallow shoulder in the potential plot. In practice the candidate critical-point intervals are locally refined until the ordering of the extrema and the signs of the barrier depths stabilize. The cavity then persists under sufficiently small variations of $(g, \alpha)$ because the three extrema remain isolated away from the phase boundary, so the cavity region is open in parameter space.

The phase map in Fig. 4 is built by applying the above criterion across a grid in $(g, \alpha)$ for fixed $M = 1$ and $\ell = 2$. Each sampled point is classified as single-barrier

when the exterior derivative exhibits only one maximum-producing sign change, and as double-peak when three sign changes producing the pattern maximum–minimum–maximum are present together with the height test (3.19). The numerical boundary is therefore the locus where the interior critical-point structure changes. Figures 2 and 3 show the representative transition at fixed $g = 0.7$, while Fig. 5 tracks the critical radii and barrier depths after cavity formation.

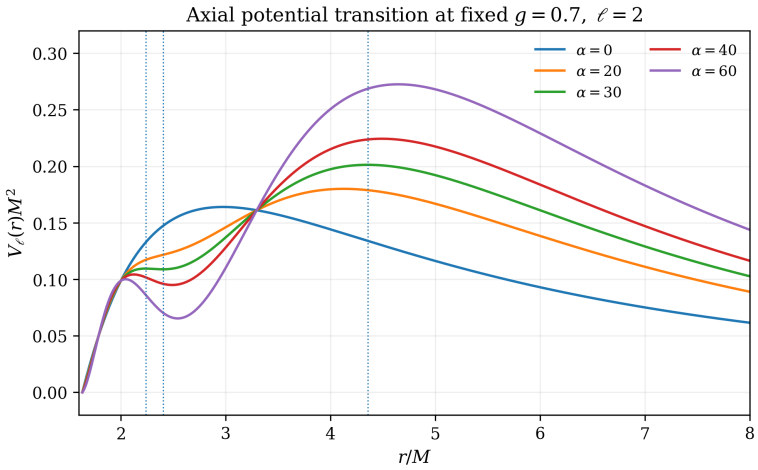



**Fig. 2** Transition of the exact axial potential at fixed $M = 1$, $g = 0.7$, and $\ell = 2$ as the deformation parameter varies. The curves correspond to $\alpha = 0, 20, 30, 40, 60$. The dotted vertical lines mark the inner maximum, the intermediate minimum, and the outer maximum for the representative cavity-producing point $\alpha = 30$. At that onset point the inner barrier height is only $\Delta V_{\rm in} \simeq 6.3 \times 10^{-4}$ above the local minimum, so the transition is genuine and at the same time shallow. The figure illustrates the precise topological change that underlies the phase classification: a single exterior barrier evolves into a max–min–max profile once the additional interior critical points appear.

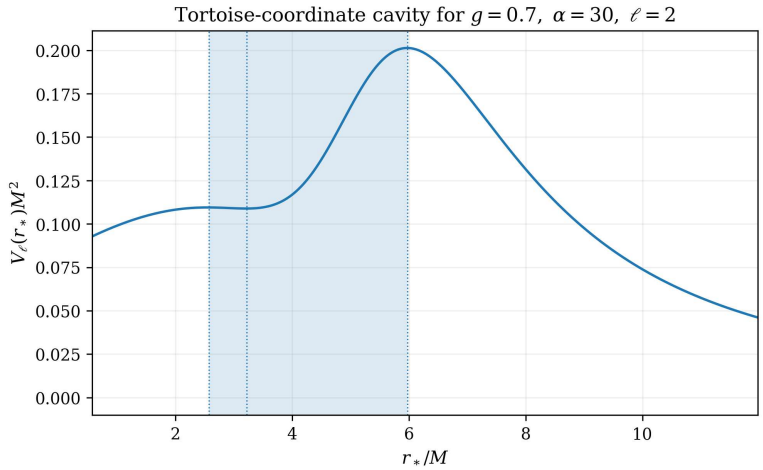



**Fig. 3** Exact axial potential in tortoise coordinate for the representative point $(M, g, \alpha, \ell) = (1, 0.7, 30, 2)$. The shaded interval is bounded by the two exterior maxima and visualizes the trapping region in the coordinate that governs wave propagation. The tortoise-coordinate picture is the relevant one for time-domain delay estimates because the cavity travel time is an integral in $r_*$.

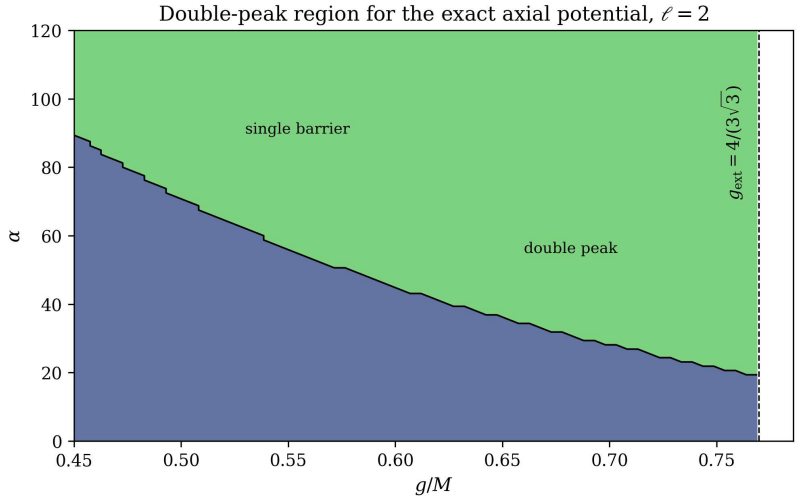



**Fig. 4** Phase map of the exact axial potential for $M = 1$ and $\ell = 2$ in the $(g, \alpha)$ plane. The lower region contains a single exterior barrier. The upper region contains three exterior critical points with the pattern maximum–minimum–maximum and therefore a genuine trapping cavity in the sense of (3.18) and (3.19). The plotted boundary is extracted from the sampled $(g, \alpha)$ grid; its step-like appearance reflects discrete sampling of the exact potential family rather than a physical non-smoothness of the transition itself. The dashed vertical line marks the extremal Hayward value $g_{\rm ext} = 4/(3\sqrt{3})$, beyond which the seed ceases to possess an event horizon.

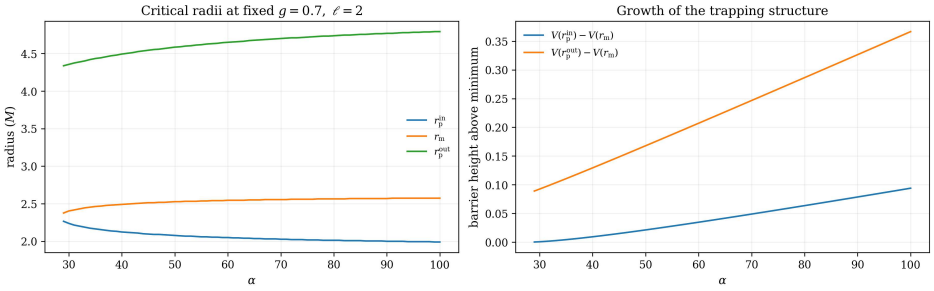



**Fig. 5** Evolution of the trapping structure after cavity formation for fixed $M = 1$, $g = 0.7$, and $\ell = 2$. The left panel shows the positions of the inner maximum, minimum, and outer maximum as functions of $\alpha$. The right panel shows the barrier heights measured relative to the intermediate minimum. These curves quantify how the cavity deepens after onset and show that the outer barrier grows more rapidly than the inner one in the displayed range.

# 4 Time-domain signal and echo scale

The frequency-domain potential analysis identifies the geometric source of delayed pulses. The time-domain problem determines how that structure is sampled by propagation. Restoring time dependence, the master equation is

$$-\frac{\partial^2\Psi}{\partial t^2} + \frac{\partial^2\Psi}{\partial r_*^2} - V_\ell(r)\Psi = 0. \tag{4.1}$$

Introduce double-null coordinates

$$u = t - r_*, \qquad v = t + r_*, \tag{4.2}$$

so that

$$\partial_t = \partial_u + \partial_v, \qquad \partial_{r_*} = -\partial_u + \partial_v. \tag{4.3}$$

A direct expansion gives

$$-\partial_t^2 + \partial_{r_*}^2 = -(\partial_u + \partial_v)^2 + (-\partial_u + \partial_v)^2 = -4\partial_u\partial_v. \tag{4.4}$$

Hence (4.1) becomes

$$4\,\partial_u\partial_v\Psi(u,v) + V_\ell\big(r(u,v)\big)\Psi(u,v) = 0. \tag{4.5}$$

Consider a null cell with corners

$$S = (u,v), \qquad E = (u, v+\Delta), \qquad W = (u+\Delta, v), \qquad N = (u+\Delta, v+\Delta). \tag{4.6}$$

Integrating (4.5) over the square gives

$$4\left[\Psi_N - \Psi_E - \Psi_W + \Psi_S\right] + \int_u^{u+\Delta} d\tilde{u} \int_v^{v+\Delta} d\tilde{v}\, V\big(r(\tilde{u},\tilde{v})\big)\Psi(\tilde{u},\tilde{v}) = 0. \tag{4.7}$$

Approximating the integral to second-order global accuracy by evaluating $V$ at the south point and $\Psi$ by the trapezoidal average of the east and west values gives

$$\int_u^{u+\Delta} d\tilde{u} \int_v^{v+\Delta} d\tilde{v}\, V\Psi = \frac{\Delta^2}{2} V_S \left(\Psi_W + \Psi_E\right) + \mathcal{O}(\Delta^4). \tag{4.8}$$

Substitution into (4.7) yields the Gundlach–Price–Pullin update

$$\Psi_N = \Psi_W + \Psi_E - \Psi_S - \frac{\Delta^2}{8} V_S \left(\Psi_W + \Psi_E\right) + \mathcal{O}(\Delta^4). \tag{4.9}$$

The local truncation error is fourth order and the accumulated waveform error is second order, which is exactly the order tested numerically in Appendix D.

The geometric delay associated with a simple max–min–max cavity is most transparently written as the round-trip time between the two exterior maxima,

$$\Delta t_{\rm cav} \simeq 2\left[r_*(r_{\rm p}^{\rm out}) - r_*(r_{\rm p}^{\rm in})\right] = 2\int_{r_{\rm p}^{\rm in}}^{r_{\rm p}^{\rm out}} \frac{dr}{\mu(r)\sqrt{1+\alpha\Xi(r)}}. \tag{4.10}$$

It is worth stating explicitly that the identification of this time difference with a difference of tortoise coordinates applies to radial null propagation, that is, to propagation at fixed angular coordinates $\theta$ and $\phi$; only then does the exact metric reduce to the two-dimensional form $ds^2 \propto -dt^2 + dr_*^2$ for which coordinate time intervals equal tortoise-coordinate intervals along null rays. This quantity is geometric and exact once the critical radii are specified. It is also a lower propagation scale whenever the reflected packet turns around at a radius deeper than the inner outer-cavity maximum. In stronger-deformation cases the potential may acquire additional shallow near-horizon structure while the outer cavity remains present. Then the relevant delay depends on the packet-dependent turning point $r_{\rm tp}$,

$$\Delta t_{\rm turn} \simeq 2\int_{r_{\rm tp}}^{r_{\rm p}^{\rm out}} \frac{dr}{\mu(r)\sqrt{1+\alpha\Xi(r)}}, \qquad r_H < r_{\rm tp} < r_{\rm p}^{\rm out}. \tag{4.11}$$

Because the tortoise map stretches logarithmically near the horizon, even a modest inward shift of $r_{\rm tp}$ can produce a visible increase in the observed pulse spacing.

For the representative characteristic evolution we take

$$M = 1, \qquad g = 0.76, \qquad \alpha = 100, \qquad \ell = 2, \tag{4.12}$$

and impose Gaussian characteristic data,

$$\Psi(u=0,v) = \exp\left[-\frac{(v-v_c)^2}{2\sigma^2}\right], \qquad \Psi(u, v=0) = 0, \tag{4.13}$$

with

$$v_c = 20M, \qquad \sigma = 2M, \qquad r_*^{\rm obs} = 40M. \tag{4.14}$$

Appendix D describes the construction of the tortoise map, the interpolation used to obtain $r(r_*)$, the null-grid implementation of the exact potential, and the convergence and robustness diagnostics.

The delayed-pulse identification rule is fixed once and used throughout the numerical discussion. For a waveform extracted at fixed $r_*^{\rm obs}$ we define $t_{\rm main}$ as the time of the largest local maximum of $|\Psi|$ in the first post-prompt ringing window, and $t_{\rm echo}$ as the time of the first subsequent local maximum of $|\Psi|$ after the signal has crossed the intermediate minimum that follows the main pulse. For the highest-resolution run with $\Delta = 0.1M$, this procedure gives

$$t_{\rm main} \approx 68.5M, \qquad t_{\rm echo} \approx 80.3M, \qquad \Delta t_{\rm obs} = t_{\rm echo} - t_{\rm main} \approx 11.8M. \tag{4.15}$$

The dominant and delayed features are shown in Fig. 6. The observed spacing exceeds the simple barrier-to-barrier estimate because the reflected packet samples a turning region shifted inward from $r_{\rm p}^{\rm in}$, exactly as suggested by (4.11). The paper therefore interprets the delayed feature as a geometry-driven secondary pulse associated with temporary trapping in the exact potential, while keeping clear that a full spectral decomposition lies beyond the present scope.

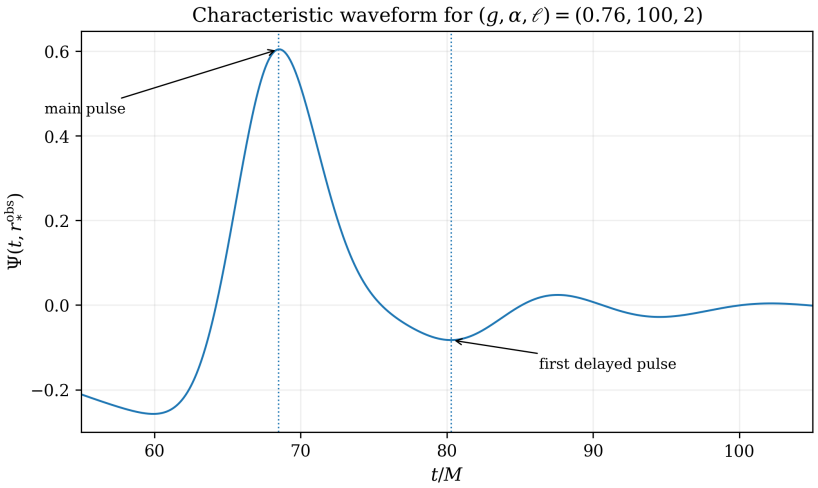



**Fig. 6** Reference characteristic waveform for the cavity-producing point $(M, g, \alpha, \ell) = (1, 0.76, 100, 2)$ with Gaussian characteristic data (4.13) and extraction at $r_*^{\rm obs} = 40M$. The dotted lines mark the dominant pulse and the first delayed secondary feature selected by the absolute-value local-maximum criterion described in the text. The waveform itself is plotted as $\Psi(t, r_*^{\rm obs})$, while the identification of the marked times is performed on the corresponding local extrema of $|\Psi|$ after the post-main-pulse intermediate minimum is crossed. The measured separation is $\Delta t_{\rm obs} \approx 11.8M$.

# 5 Discussion

The analysis developed in this work identifies a concrete geometric mechanism through which a regular black-hole seed, once embedded in a radially deformed anisotropic

environment, can acquire an exterior odd-parity trapping structure capable of supporting delayed secondary pulses. The central value of the construction lies in the fact that the background sector remains exact throughout. The Hayward seed is carried into the deformed configuration by a closed-form radial minimal geometric deformation, the Einstein system separates cleanly into seed and decoupler blocks, the admissibility condition for horizon inheritance is explicit, and the near-center expansion shows finite orthonormal curvature components and finite curvature invariants. At the level relevant for perturbation theory, this places the entire analysis on a background that is analytically controlled from the center to the asymptotic region.

The background results also clarify the precise status of regularity in the present model. The metric functions remain finite at the center and the curvature scalars approach finite limits, so the geometry is curvature regular in the strict invariant sense used in the paper. The center, however, carries deformation-dependent radial corrections beyond the even-order structure of the undeformed seed. That feature matters conceptually because it distinguishes the present deformed geometry from the more restrictive notion of an exact maximally symmetric core. The discussion of regularity therefore enters the perturbative problem through a well-defined statement: the geometry supplies a smooth enough and invariantly finite background for the axial analysis, while still retaining a deformation-sensitive short-distance structure that contributes to the reshaping of the effective potential.

A second central outcome is the exact decomposition of the odd-parity potential. Once the frozen-source axial closure is fixed, the master equation takes the Schrödinger form with a potential whose two contributions can be read directly from the geometry. The seed part carries the full imprint of the nonvacuum Hayward background through the matter-sensitive term proportional to $m'_H(r)$, while the deformation profile contributes an additional exact piece proportional to the radial MGD sector. This separation is physically informative because it isolates two distinct mechanisms inside the same geometry: the regularity scale controls how the seed departs from the vacuum Schwarzschild pattern, and the decoupling profile controls how that regular seed is reshaped in the exterior domain. The cavity-producing regime emerges from the combined action of these two ingredients.

That mechanism is particularly clear near the onset of the double-peak region. The representative point studied in the manuscript lies close to the transition where a single exterior barrier splits into the ordered maximum–minimum–maximum pattern required for temporary trapping. The numerical values show that the inner barrier can be extremely shallow at onset, while the outer barrier is already appreciable. This is an important physical and numerical feature. Physically, it shows that cavity formation begins as a delicate reorganization of the near-horizon side of the potential before the outer trapping structure deepens further. Numerically, it means that the phase classification must be based on refined root isolation and an explicit positive-height test rather than on visual inspection alone. The resulting phase map therefore carries a precise interpretation: it charts the region in which the exact potential family possesses the ordered critical-point structure required for axial trapping.

The tortoise-coordinate picture provides the natural language for understanding why that structure matters dynamically. Once the potential is viewed as a function of

$r_*$, the two exterior maxima bound an interval in the propagation coordinate itself, so the cavity travel time becomes an integral property of the geometry. In that sense the delayed-pulse mechanism discussed here is geometric from the start. No external mirror, junction surface, or phenomenological reflection condition is introduced by hand. The relevant travel scales are already encoded in the exact metric functions through the tortoise map. This point is conceptually important because it ties delayed structure directly to the background solution and gives the axial potential a dual role: it governs both frequency-domain scattering and the coordinate-space travel times that shape the time-domain signal.

The characteristic evolution then supplies a representative dynamical realization of that geometric picture. The numerical sector is framed conservatively in the manuscript, and that conservative framing is one of its strengths. The extracted delayed feature is presented as representative evidence tied to a cavity-producing background, the pulse-identification rule is stated in terms of local maxima of $|\Psi|$, and the reported spacing is accompanied by convergence and robustness tests. The observed delay exceeds the simplest barrier-to-barrier round-trip scale, which is exactly the behavior expected when the reflected packet samples a turning region lying deeper than the inner outer-cavity maximum. The comparison between the measured spacing and the geometric lower scale therefore supports a coherent interpretation: the delayed structure probes the same deformed potential that produced the cavity in the first place, while the precise spacing depends on where the wave packet turns around inside that geometry.

The scope of the perturbative claim is also sharply delimited by the axial closure adopted in the paper. The working assumption is that the effective source supporting the background introduces no independent propagating odd-parity degree of freedom, so the odd sector is carried entirely by the metric once the background coefficients are fixed. Within that framework the manuscript establishes an internally complete axial calculation. This gives the results a clear status: the exact background construction, the exact axial potential, the onset of the cavity region, and the representative delayed-pulse signal belong to one common perturbative framework. That clarity is valuable because it lets the reader identify precisely which parts of the analysis are theorem-level statements inside the adopted closure and which parts are representative numerical manifestations of the same structure.

The paper also occupies a specific place in the existing literature. Within perturbative studies of regular black holes, the present contribution is centered on an already regular Hayward seed that is then dressed by an exact radial minimal geometric deformation. Within the gravitational-decoupling literature, the relevant contribution is the identification of a closed-form regular-seed-plus-deformation geometry whose axial potential can be written as an explicit sum of a nonvacuum seed term and a deformation term. This mechanism-level distinction matters for how the results should be read. The manuscript does more than observe that multibarrier potentials can produce delayed features. It shows, within one exact background family, how a regularity scale and a deformation profile cooperate to generate that multibarrier structure.

From a broader perspective, the results should be stated with care regarding what is and is not established about the role of regularity. What the analysis demonstrates is a correlation, within the frozen-source axial closure, between the presence of the

regularity scale and the formation of the exterior trapping cavity: the seed contribution to the exact potential carries the matter-sensitive term proportional to $m'_H(r)$, both that term and the deformation profile are controlled by $g$, and the cavity-producing region of the phase map occupies only a restricted part of the $(g, \alpha)$ plane rather than the whole admissible domain. The evidence presented here therefore does not support the stronger causal statement that regularity by itself drives the delayed signals; the cavity requires the combined action of the regularity scale and a sufficiently strong deformation, and it is absent in large portions of parameter space, including at small $\alpha$ for any $g$. Accordingly, the appropriate reading of the mechanism is that short-distance regularity and exterior trapping are correlated within this exact deformed family, in the precise sense charted by the phase map, while a causal attribution would require evidence beyond the scope of the present study, such as a systematic comparison across regular and singular seeds under the same deformation.

Several natural continuations follow from the present results. A frequency-domain quasinormal-mode and quasi-bound-state analysis would reveal how the cavity structure is encoded in the complex spectrum of the exact potential family. A polar-sector treatment would determine how much of the present mechanism survives beyond the odd-parity channel; the reason it was not pursued here is structural rather than practical. In the axial sector the static, diagonal, parity-even effective source supports the frozen-source closure, so the metric perturbation evolves alone and the problem reduces to one exact master equation. In the polar sector the even-parity metric functions couple directly to the perturbations of the effective density and pressures already at the level of the constraint equations, so an analogous simplification is not available: one must specify how the decoupler sector itself fluctuates, for example through an equation of state or a field-theoretic completion, and the reduction generically yields a coupled system rather than a single potential. The anticipated bottleneck is therefore the model dependence introduced by the polar matter sector, which would dilute the sharp, assumption-light character that the axial analysis enjoys in the present setting. A higher-resolution study of the phase boundary would sharpen the onset geometry of the cavity-producing region. An observational follow-up could then ask how the cavity phase map projects into time-domain waveform diagnostics and whether families of delayed features can be parameterized directly in terms of the regularity scale and deformation strength. Each of these directions grows naturally out of the present framework because the background solution, the perturbative reduction, and the numerical methodology are already organized in a form suitable for extension.

In summary, the manuscript establishes a coherent chain from exact geometry to perturbative structure and then to representative wave propagation. The Hayward seed supplies a curvature-regular starting point, radial minimal geometric deformation reshapes that seed in closed form, the resulting background generates an exact axial potential with analytically separable contributions, and an open region of parameter space supports the max–min–max structure required for temporary trapping. The time-domain evolution then shows how that structure can manifest itself through delayed secondary pulses. Taken together, these results identify a precise and geometrically controlled route by which regular black-hole backgrounds in the decoupling framework can acquire observationally relevant late-time structure in the axial gravitational channel.

## Author contributions

All authors contributed equally to the conceptual development, derivations, writing, and revision of the manuscript.

## Data Availability

No external data set was used in this work.

## Competing interests

The authors declare no competing interests.

## Ethical Considerations

The authors have diligently addressed ethical concerns, such as informed consent, plagiarism, data fabrication, misconduct, falsification, double publication, redundancy, submission, and other related matters.

## Funding

This research received no external funding.

## References

[1] R. Penrose, Gravitational collapse and space-time singularities, Phys. Rev. Lett. **14**, 57 (1965).

[2] S. W. Hawking and R. Penrose, The singularities of gravitational collapse and cosmology, Proc. Roy. Soc. Lond. A **314**, 529 (1970).

[3] S. W. Hawking and G. F. R. Ellis, *The Large Scale Structure of Space-Time* (Cambridge University Press, Cambridge, 1973).

[4] J. M. Bardeen, Non-singular general-relativistic gravitational collapse, in *Proceedings of the International Conference GR5*, Tbilisi, U.S.S.R. (1968).

[5] I. Dymnikova, Vacuum nonsingular black hole, Gen. Relativ. Gravit. **24**, 235 (1992).

[6] E. Ayón-Beato and A. García, Regular black hole in general relativity coupled to nonlinear electrodynamics, Phys. Rev. Lett. **80**, 5056 (1998).

[7] E. Ayón-Beato and A. García, The Bardeen model as a nonlinear magnetic monopole, Phys. Lett. B **493**, 149 (2000).

[8] K. A. Bronnikov, Regular magnetic black holes and monopoles from nonlinear electrodynamics, Phys. Rev. D **63**, 044005 (2001).

[9] S. A. Hayward, Formation and evaporation of nonsingular black holes, Phys. Rev. Lett. **96**, 031103 (2006).

[10] S. Ansoldi, Spherical black holes with regular center: A review of existing models including a recent realization with Gaussian sources, in *Conference on Black Holes and Naked Singularities*, edited by R. Kerner, R. B. Mann, and D. Winstanley, arXiv:0802.0330 [gr-qc].

[11] C. Bambi and L. Modesto, Rotating regular black holes, Phys. Lett. B **721**, 329 (2013).

[12] V. P. Frolov, Notes on non-singular models of black holes, Phys. Rev. D **94**, 104056 (2016).

[13] T. Harada, C.-M. Chen, and R. Mandal, Singularity resolution and regular black hole formation in gravitational collapse in asymptotically safe gravity, arXiv:2502.16787 [gr-qc].

[14] S. Gielen and L. Menéndez-Pidal, Black hole singularity resolution in unimodular gravity from unitarity, Phys. Rev. Lett. **134**, 101501 (2025).

[15] P. Bueno, P. A. Cano, R. A. Hennigar, Á. J. Murcia, and A. Vicente-Cano, Regular black holes from Oppenheimer–Snyder collapse, arXiv:2505.09680 [gr-qc].

[16] A. Bonanno, R. A. Konoplya, G. Oglialoro, and A. Spina, Regular black holes from proper-time flow in quantum gravity and their quasinormal modes, shadow and Hawking radiation, JCAP **12**, 042 (2025).

[17] N. Bukowiecka, A. Ricarte, P. Kocherlakota, and C. Prather, On the observational distinguishability of the Kerr and Kerr-Hayward metrics to the Event Horizon Telescope, arXiv:2604.06128 [astro-ph.HE].

[18] D. M. Capper, M. Liu, and A. Saini, No-go theorem for singularity resolution, arXiv:2604.00204 [gr-qc].

[19] C. A. R. Herdeiro and E. Radu, Asymptotically flat black holes with scalar hair: A review, Int. J. Mod. Phys. D **24**, 1542014 (2015).

[20] J. Ovalle, Decoupling gravitational sources in general relativity: From perfect to anisotropic fluids, Phys. Rev. D **95**, 104019 (2017).

[21] J. Ovalle, The minimal geometric deformation approach: a brief introduction, Phys. Lett. B **788**, 213 (2019).

[22] J. Ovalle, R. Casadio, and A. Sotomayor, Black holes by gravitational decoupling, Eur. Phys. J. C **78**, 122 (2018).

[23] J. Ovalle, E. Contreras, and R. Casadio, The decoupling method in general relativity, Phys. Dark Univ. **31**, 100744 (2021).

[24] R. Avalos, P. Bargueño, and E. Contreras, Exact anisotropic solutions by gravitational decoupling: A review, Fortschr. Phys. **71**, 2200171 (2023).

[25] R. Avalos and E. Contreras, Hairy black holes by gravitational decoupling, Eur. Phys. J. C **83**, 155 (2023).

[26] F. Tello-Ortiz, E. Contreras, and Á. Rincón, Anisotropic black holes and compact objects in gravitational decoupling, Eur. Phys. J. C **83**, 796 (2023).

[27] Y. Hua, Z. Ban, T.-Y. Ren, J.-J. Yin, and R.-J. Yang, Regular hairy black holes through gravitational decoupling method, arXiv:2510.20524 [gr-qc].

[28] Y. Hua and R.-J. Yang, Nonsingular hairy black holes by gravitational decoupling, arXiv:2512.20320 [gr-qc].

[29] Y. Yang, A. Övgün, G. Lambiase, D. Liu, and Z.-W. Long, Axial gravitational perturbations and echo-like signals of a hairy black hole from gravitational decoupling, arXiv:2604.02164 [gr-qc].

[30] T. Regge and J. A. Wheeler, Stability of a Schwarzschild singularity, Phys. Rev. **108**, 1063 (1957).

[31] F. J. Zerilli, Effective potential for even-parity Regge–Wheeler gravitational perturbation equations, Phys. Rev. Lett. **24**, 737 (1970).

[32] C. V. Vishveshwara, Scattering of gravitational radiation by a Schwarzschild black-hole, Nature **227**, 936 (1970).

[33] S. Chandrasekhar and V. Ferrari, On the non-radial oscillations of a star, Proc. Roy. Soc. Lond. A **432**, 247 (1991).

[34] E. W. Leaver, An analytic representation for the quasi-normal modes of Kerr black holes, Proc. Roy. Soc. Lond. A **402**, 285 (1985).

[35] B. F. Schutz and C. M. Will, Black hole normal modes: A semianalytic approach, Astrophys. J. Lett. **291**, L33 (1985).

[36] S. Iyer and C. M. Will, Black-hole normal modes: A WKB approach. I. Foundations and application of a higher-order WKB analysis of potential-barrier scattering, Phys. Rev. D **35**, 3621 (1987).

[37] H.-P. Nollert, Quasinormal modes: the characteristic 'sound' of black holes and neutron stars, Class. Quant. Grav. **16**, R159 (1999).

[38] K. D. Kokkotas and B. G. Schmidt, Quasi-normal modes of stars and black holes, Living Rev. Rel. **2**, 2 (1999).

[39] E. Berti, V. Cardoso, and A. O. Starinets, Quasinormal modes of black holes and black branes, Class. Quant. Grav. **26**, 163001 (2009).

[40] R. A. Konoplya and A. Zhidenko, Quasinormal modes of black holes: From astrophysics to string theory, Rev. Mod. Phys. **83**, 793 (2011).

[41] R. A. Konoplya, Quasinormal behavior of the D-dimensional Schwarzschild black hole and higher order WKB approach, Phys. Rev. D **68**, 024018 (2003).

[42] J. Matyjasek and M. Opala, Quasinormal modes of black holes. The improved semianalytic approach, Phys. Rev. D **96**, 024011 (2017).

[43] A. Jansen, Overdamped modes in Schwarzschild–de Sitter and a Mathematica package for the numerical computation of quasinormal modes, Eur. Phys. J. Plus **132**, 546 (2017).

[44] M. Srivastava, Y. Chen, and S. Shankaranarayanan, Analytical computation of quasinormal modes of slowly rotating black holes in dynamical Chern–Simons gravity, Phys. Rev. D **104**, 064034 (2021), arXiv:2106.06209 [gr-qc].

[45] S. Dhanpal, A. Ghosh, A. K. Mehta, P. Ajith, and B. S. Sathyaprakash, A "no-hair" test for binary black holes, Phys. Rev. D **99**, 104056 (2019), arXiv:1804.03297 [gr-qc].

[46] C. Gundlach, R. H. Price, and J. Pullin, Late-time behavior of stellar collapse and explosions: I. Linearized perturbations, Phys. Rev. D **49**, 883 (1994).

[47] B. P. Abbott *et al.* (LIGO Scientific Collaboration and Virgo Collaboration), Observation of gravitational waves from a binary black hole merger, Phys. Rev. Lett. **116**, 061102 (2016).

[48] E. Berti, V. Cardoso, and C. M. Will, Gravitational-wave spectroscopy of massive black holes with the space interferometer LISA, Phys. Rev. D **73**, 064030 (2006).

[49] V. Cardoso, E. Franzin, and P. Pani, Is the gravitational-wave ringdown a probe of the event horizon?, Phys. Rev. Lett. **116**, 171101 (2016); Erratum Phys. Rev. Lett. **117**, 089902 (2016).

[50] J. Abedi, H. Dykaar, and N. Afshordi, Echoes from the abyss: Tentative evidence for Planck-scale structure at black hole horizons, Phys. Rev. D **96**, 082004 (2017).

[51] Z. Mark, A. Zimmerman, S. M. Du, and Y. Chen, A recipe for echoes from exotic compact objects, Phys. Rev. D **96**, 084002 (2017).

[52] J. Westerweck *et al.*, Low significance of evidence for black hole echoes in gravitational wave data, Phys. Rev. D **97**, 124037 (2018).

[53] V. Cardoso and P. Pani, Testing the nature of dark compact objects: A status report, Living Rev. Rel. **22**, 4 (2019).

[54] R. S. Conklin and B. Holdom, Gravitational wave echo spectra, Phys. Rev. D **100**, 124030 (2019), arXiv:1905.09370 [gr-qc].

[55] S. Xin, B. Chen, R. K. L. Lo, L. Sun, W.-B. Han, X. Zhong, M. Srivastava, S. Ma, Q. Wang, and Y. Chen, Gravitational-wave echoes from spinning exotic compact objects: Numerical waveforms from the Teukolsky equation, Phys. Rev. D **104**, 104005 (2021), arXiv:2105.12313 [gr-qc].

[56] M. Srivastava and Y. Chen, Gravitational radiation close to a black hole horizon: Waveform regularization and the out-going echo, Phys. Rev. D **104**, 104006 (2021), arXiv:2108.01329 [gr-qc].

[57] M. Skvortsova, Ringing of the extreme regular black holes, Grav. Cosmol. **30**, 279 (2024).

[58] Z. Malik, Gravitational perturbations of the Hayward spacetime and testing the correspondence between quasinormal modes and greybody factors, Int. J. Theor. Phys. **64**, 314 (2025).

[59] M. Colpi *et al.*, LISA definition study report, arXiv:2402.07571 [astro-ph.CO].

[60] M. Maggiore *et al.*, Science case for the Einstein Telescope, JCAP **03**, 050 (2020).

# A Field equations for the static spherical ansatz

This appendix records the static-spherical geometry formulas used in the main text. For the metric

$$ds^2 = -A(r)\,dt^2 + \frac{dr^2}{B(r)} + r^2\left(d\theta^2 + \sin^2\theta\,d\phi^2\right), \tag{A.1}$$

the nonvanishing Christoffel symbols are

$$\begin{aligned}
&\Gamma^t{}_{tr} = \frac{A'}{2A}, && \Gamma^r{}_{tt} = \frac{BA'}{2}, && \Gamma^r{}_{rr} = -\frac{B'}{2B},\\
&\Gamma^r{}_{\theta\theta} = -Br, && \Gamma^r{}_{\phi\phi} = -Br\sin^2\theta, && \Gamma^\theta{}_{r\theta} = \Gamma^\phi{}_{r\phi} = \frac{1}{r},\\
&\Gamma^\theta{}_{\phi\phi} = -\sin\theta\cos\theta, && \Gamma^\phi{}_{\theta\phi} = \cot\theta. &&
\end{aligned} \tag{A.2}$$

A straightforward computation of the Ricci tensor gives

$$R_{tt} = \frac{BA''}{2} + \frac{A'B'}{4} + \frac{BA'}{r} - \frac{B(A')^2}{4A}, \tag{A.3}$$

$$R_{rr} = -\frac{A''}{2A} - \frac{A'B'}{4AB} - \frac{A'}{Ar} - \frac{B'}{Br} + \frac{(A')^2}{4A^2}, \tag{A.4}$$

$$R_{\theta\theta} = 1 - B - \frac{rB'}{2} - \frac{rBA'}{2A}, \qquad R_{\phi\phi} = \sin^2\theta\,R_{\theta\theta}. \tag{A.5}$$

Contracting with the inverse metric yields the Ricci scalar

$$R = -B\frac{A''}{A} + \frac{B}{2}\left(\frac{A'}{A}\right)^2 - \frac{A'B'}{2A} - \frac{2BA'}{Ar} - \frac{2B'}{r} + \frac{2(1-B)}{r^2}. \tag{A.6}$$

Using $G_{\mu\nu} = R_{\mu\nu} - \frac{1}{2}g_{\mu\nu}R$ and $T^\mu{}_\nu = \mathrm{diag}[-\rho, p_r, p_t, p_t]$, one recovers the equations quoted in the main text,

$$8\pi\rho = \frac{1-B}{r^2} - \frac{B'}{r}, \tag{A.7}$$

$$8\pi p_r = -\frac{1-B}{r^2} + \frac{B}{r}\frac{A'}{A}, \tag{A.8}$$

$$8\pi p_t = \frac{B}{2}\frac{A''}{A} - \frac{B}{4}\left(\frac{A'}{A}\right)^2 + \frac{B'}{4}\frac{A'}{A} + \frac{B}{2r}\frac{A'}{A} + \frac{B'}{2r}. \tag{A.9}$$

The conservation equation follows from $\nabla_\mu T^\mu{}_r = 0$ and gives

$$p_r' + \frac{A'}{2A}(\rho + p_r) + \frac{2}{r}(p_r - p_t) = 0. \tag{A.10}$$

## B Expanded near-center curvature analysis

The regularity proof in the main text is driven by the center expansions of $A$ and $B$. This appendix records the algebra in a slightly expanded form. Starting from

$$\mu(r) = 1 - \frac{2Mr^2}{r^3 + 2Mg^2}, \tag{B.1}$$

one rewrites the fraction as

$$\frac{2Mr^2}{r^3 + 2Mg^2} = \frac{r^2}{g^2} \frac{1}{1 + r^3/(2Mg^2)}. \tag{B.2}$$

Expanding the denominator by the geometric series,

$$\frac{1}{1+x} = 1 - x + x^2 + \mathcal{O}(x^3), \qquad x = \frac{r^3}{2Mg^2}, \tag{B.3}$$

gives

$$\mu(r) = 1 - \frac{r^2}{g^2} + \frac{r^5}{2Mg^4} + \mathcal{O}(r^8). \tag{B.4}$$

For the deformation factor,

$$\Xi(r) = 16g^2r^2(r-2M)^2(r^2+g^2)^{-3}, \tag{B.5}$$

we use

$$(r-2M)^2 = 4M^2 - 4Mr + r^2, \qquad (r^2+g^2)^{-3} = g^{-6}\left(1 + \frac{r^2}{g^2}\right)^{-3}. \tag{B.6}$$

Since $(1+y)^{-3} = 1 - 3y + \mathcal{O}(y^2)$, one finds

$$\Xi(r) = \frac{64M^2}{g^4}r^2 - \frac{64M}{g^4}r^3 + \mathcal{O}(r^4). \tag{B.7}$$

Combining (B.4) and (B.7) yields

$$B(r) = \mu(r)\left[1 + \alpha\Xi(r)\right] = 1 + \left(-\frac{1}{g^2} + \frac{64\alpha M^2}{g^4}\right)r^2 - \frac{64\alpha M}{g^4}r^3 + \mathcal{O}(r^4). \tag{B.8}$$

The orthonormal Riemann components then follow from the formulas in the main text. Their limits are finite because the potentially singular denominators $1/r$ and $1/r^2$ are cancelled by the leading behavior of $\nu'$ and $1 - B$. Explicitly,

$$\frac{B\nu'}{2r} = a_2 + \mathcal{O}(r), \qquad \frac{B'}{2r} = b_2 + \mathcal{O}(r), \qquad \frac{1-B}{r^2} = -b_2 + \mathcal{O}(r). \tag{B.9}$$

This is why the invariants remain finite even though $B(r)$ contains an odd cubic correction. The cubic term shifts subleading coefficients and therefore distinguishes the deformed center from an exact maximally symmetric core, yet it leaves the curvature-regular character intact.

# C Odd-parity reduction and phase-map criterion

This appendix records the reduction used to obtain the axial master equation and the numerical classification criterion used in the phase map. The working assumption is that the effective source supporting the background carries no independent odd-parity propagating degree of freedom. At the level of linearized field equations this means that the odd sector is evaluated with vanishing source perturbation, so the role of the matter sector is exhausted by the background coefficients already contained in $A(r)$ and $B(r)$. For a static diagonal anisotropic source this is the standard axial closure used in perturbation theory when no extra axial matter variable is introduced explicitly [33]. The separation of the radial problem from the angular dependence proceeds in the standard way [30, 33, 38]. The odd-parity perturbation (3.1) is built from the axial vector harmonics; restricting to $m = 0$ as justified in the main text, their only nonvanishing components are proportional to $\sin\theta\,\partial_\theta P_\ell(\cos\theta)$. The linearized Einstein equations are then projected onto this angular basis: the $(t\phi)$ and $(r\phi)$ components of the perturbed field equations each factor into the common angular function $\sin\theta\,\partial_\theta P_\ell(\cos\theta)$ multiplying a purely radial expression, once the Legendre identity (3.2) is used to eliminate second angular derivatives in favor of the eigenvalue $\ell(\ell+1)$. Setting the radial factors to zero yields two first-order equations relating $h_0$ and $h_1$, while the $(\theta\phi)$ component supplies the algebraic compatibility relation between them. Eliminating $h_0$ between these equations produces the single second-order radial equation quoted below; no angular dependence survives because every term carries the same harmonic factor. Under that closure the linearized Einstein system for the Regge–Wheeler gauge perturbations (3.1) reduces to the standard two-equation axial system familiar from the perturbation theory of static fluid backgrounds. After harmonic decomposition one can eliminate $H_0(r)$ in favor of $H_1(r)$ and obtain a second-order radial equation of the form

$$\frac{d^2H_1}{dr^2} + P(r)\frac{dH_1}{dr} + Q(r)H_1 + \omega^2\frac{H_1}{A(r)B(r)} = 0, \tag{C.1}$$

where

$$P(r) = \frac{1}{2}\left(\frac{A'}{A} + \frac{B'}{B}\right) - \frac{2}{r} \tag{C.2}$$

and the nonderivative coefficient can be arranged as

$$Q(r) = -\frac{1}{A(r)B(r)}\left[A(r)\left(\frac{\ell(\ell+1)}{r^2} + \frac{2(B(r)-1)}{r^2}\right) - \frac{A(r)B'(r) + B(r)A'(r)}{2r}\right]. \tag{C.3}$$

Introducing the tortoise coordinate and the rescaled master field

$$\frac{dr_*}{dr} = \frac{1}{\sqrt{A(r)B(r)}}, \qquad \Psi(r) = \frac{\sqrt{A(r)B(r)}}{r} H_1(r), \tag{C.4}$$

removes the first derivative and converts (C.1) into

$$\frac{d^2\Psi}{dr_*^2} + \left[\omega^2 - V_\ell(r)\right]\Psi = 0, \tag{C.5}$$

with

$$V_\ell(r) = A(r)\left[\frac{\ell(\ell+1)}{r^2} + \frac{2(B(r)-1)}{r^2}\right] - \frac{A(r)B'(r) + B(r)A'(r)}{2r}. \tag{C.6}$$

The derivation is standard once the closure is fixed, and the formulas are recorded here to make the notation of the main text self-contained.

For the phase map a point $(g, \alpha)$ is classified numerically in the following way. First, the outer horizon $r_H$ is computed from the seed equation (2.9). Second, the exact potential is sampled on a dense exterior grid $r \in (r_H + \varepsilon, r_{\max})$ with $\varepsilon > 0$ small and $r_{\max}$ large enough to capture the asymptotic decay. Third, finite-difference derivatives are used to locate candidate sign changes of $V_\ell'(r)$ on the coarse grid. Fourth, every candidate interval is locally refined and passed to a one-dimensional root finder for $V_\ell'(r) = 0$ until the root ordering is stable under further mesh refinement. Fifth, the neighboring sign pattern of $V_\ell'$ and, when needed, the sign of $V_\ell''$ are used to distinguish maxima from minima. Sixth, the barrier depths relative to the local minimum are evaluated explicitly. A point is marked as cavity-producing only when three distinct exterior critical points exist with the ordered pattern maximum–minimum–maximum and the barrier heights above the local minimum are both strictly positive. This criterion is stricter than a visual double-hump impression and is the one used in the figures of the main text. Near the onset line the inner barrier can be extremely shallow, so the refinement and explicit height test are essential parts of the classification rather than cosmetic numerical detail.

# D Characteristic evolution, convergence, robustness, and sampled data

This appendix collects the numerical information used in the time-domain discussion. The exact wave equation in null coordinates is

$$4\,\partial_u\partial_v\Psi(u,v) + V_\ell\big(r(u,v)\big)\Psi(u,v) = 0, \tag{D.1}$$

with tortoise coordinate

$$\frac{dr_*}{dr} = \frac{1}{\mu(r)\sqrt{1+\alpha\Xi(r)}}. \tag{D.2}$$

For every fixed $(g, \alpha)$ and every admissible deformation, the map $r \mapsto r_*$ is strictly monotone on the exterior domain because the integrand is positive. The numerical

implementation therefore proceeds by sampling the exterior radial domain, evaluating the cumulative tortoise integral, and inverting the map by monotone interpolation. The exact potential is computed on that radial mesh from (3.9) and then transferred to the null grid through

$$r_* = \frac{v-u}{2}. \tag{D.3}$$

The reference characteristic data are

$$\Psi(u=0,v) = \exp\left[-\frac{(v-v_c)^2}{2\sigma^2}\right], \qquad \Psi(u,v=0) = 0, \tag{D.4}$$

with $(v_c,\sigma) = (20M, 2M)$ and extraction at $r_*^{\rm obs} = 40M$. The extraction worldline is therefore

$$v - u = 2r_*^{\rm obs}. \tag{D.5}$$

Because the diagonal index of the null grid fixes $r_*$, the potential lookup needs to be performed only once per diagonal and can then be reused throughout the evolution.

For pulse identification the extracted waveform is analyzed both as $\Psi(t, r_*^{\rm obs})$ and as $|\Psi(t, r_*^{\rm obs})|$. The main pulse is defined as the largest local maximum of $|\Psi|$ in the first post-prompt ringing window. The first delayed feature is then defined as the first subsequent local maximum of $|\Psi|$ after the waveform has crossed the intermediate minimum that follows the main pulse. This rule is the one used for the times quoted in the main text and is intentionally more precise than selecting delayed structure by eye from the oscillatory signal.

The convergence test uses three grid spacings,

$$\Delta = 0.4M, \qquad \Delta/2 = 0.2M, \qquad \Delta/4 = 0.1M. \tag{D.6}$$

After interpolation to a common time array, the measured convergence orders are

$$p_{L^2} = \log_2\left(\frac{\|\Psi_\Delta - \Psi_{\Delta/2}\|_{L^2}}{\|\Psi_{\Delta/2} - \Psi_{\Delta/4}\|_{L^2}}\right), \qquad p_{L^\infty} = \log_2\left(\frac{\|\Psi_\Delta - \Psi_{\Delta/2}\|_{L^\infty}}{\|\Psi_{\Delta/2} - \Psi_{\Delta/4}\|_{L^\infty}}\right). \tag{D.7}$$

For the reference run one finds

$$p_{L^2} \approx 2.003, \qquad p_{L^\infty} \approx 2.002, \tag{D.8}$$

which is consistent with the second-order global accuracy of the characteristic update. Figure 7 shows the waveform overlay and the scaled-difference comparison.

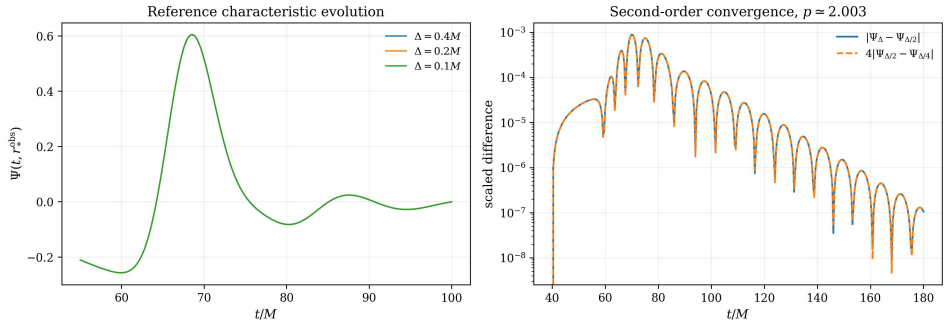



**Fig. 7** Numerical validation of the reference characteristic evolution at $(M, g, \alpha, \ell) = (1, 0.76, 100, 2)$. Left: extracted waveforms for $\Delta = 0.4M$, $0.2M$, and $0.1M$. Right: convergence test comparing $|\Psi_\Delta - \Psi_{\Delta/2}|$ with $4|\Psi_{\Delta/2} - \Psi_{\Delta/4}|$, which is the expected scaling for a globally second-order scheme.

Robustness with respect to extraction radius and initial pulse width is summarized in Tables 1 and 2. The first table changes $r_*^{\rm obs}$ while keeping the background and initial data fixed. The second changes $\sigma$ while keeping the background and extraction radius fixed. In both cases the first delayed spacing remains clustered around the quoted value, while the amplitude ratio varies with the expected change in propagation distance or spectral content.

**Table 1**: Dependence of the first delayed spacing on the extraction radius for the reference run at $\Delta = 0.1M$.

| $r_*^{\rm obs}/M$ | $t_{\rm main}/M$ | $t_{\rm echo}/M$ | $\Delta t_{\rm echo}/M$ | $\lvert\Psi_{\rm echo}\rvert/\lvert\Psi_{\rm main}\rvert$ |
|---|---|---|---|---|
| 20 | 48.7 | 60.5 | 11.8 | 0.1284 |
| 30 | 58.6 | 70.4 | 11.8 | 0.1325 |
| 40 | 68.5 | 80.3 | 11.8 | 0.1369 |
| 60 | 88.5 | 100.2 | 11.7 | 0.1444 |

**Table 2**: Dependence of the first delayed spacing on the Gaussian width $\sigma$ at fixed extraction radius $r_*^{\rm obs} = 40M$ and fixed center $v_c = 20M$.

| $\sigma/M$ | $t_{\rm main}/M$ | $t_{\rm echo}/M$ | $\Delta t_{\rm echo}/M$ | $\lvert\Psi_{\rm echo}\rvert/\lvert\Psi_{\rm main}\rvert$ |
|---|---|---|---|---|
| 1.5 | 68.4 | 80.4 | 12.0 | 0.1315 |
| 2.0 | 68.5 | 80.3 | 11.8 | 0.1369 |
| 3.0 | 68.9 | 80.3 | 11.4 | 0.1403 |
| 4.0 | 69.2 | 81.1 | 11.9 | 0.1229 |

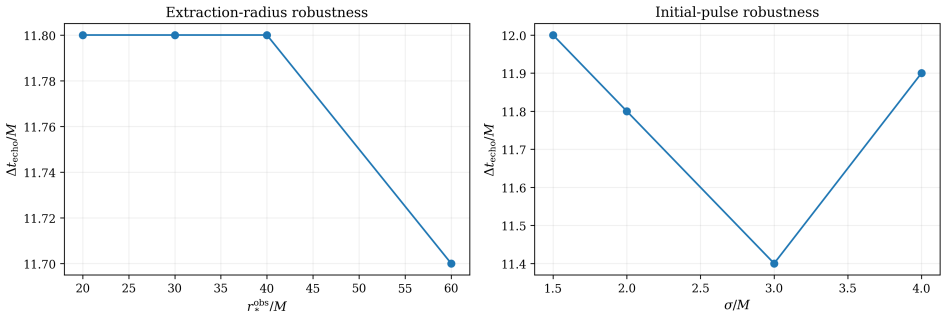



**Fig. 8** Robustness of the first delayed spacing under changes of extraction radius and under moderate changes of the Gaussian initial width. The left panel varies the observer location. The right panel varies $\sigma$ while keeping the background fixed. Both panels show that the delayed spacing remains tightly clustered around the reference value.

The geometric delay comparison for the strong-deformation point (4.12) is also explicit. The outer cavity is bounded by

$$r_{\mathrm{p}}^{\mathrm{in}} \approx 1.924M, \qquad r_{\mathrm{p}}^{\mathrm{out}} \approx 4.830M, \tag{D.9}$$

which correspond in tortoise coordinate to

$$r_*(r_{\mathrm{p}}^{\mathrm{in}}) \approx -6.472M, \qquad r_*(r_{\mathrm{p}}^{\mathrm{out}}) \approx -2.316M. \tag{D.10}$$

The barrier-to-barrier propagation scale is therefore

$$\Delta t_{\mathrm{cav}} = 2\left[r_*(r_{\mathrm{p}}^{\mathrm{out}}) - r_*(r_{\mathrm{p}}^{\mathrm{in}})\right] \approx 8.31M. \tag{D.11}$$

Compared with the measured value,

$$\Delta t_{\mathrm{obs}} \approx 11.8M, \qquad \frac{\Delta t_{\mathrm{obs}}}{\Delta t_{\mathrm{cav}}} \approx 1.42, \tag{D.12}$$

one sees directly that the observed pulse spacing exceeds the simple cavity round-trip scale. This has the expected sign because the reflected packet samples a turning region deeper than the inner outer-cavity maximum.

Finally, the sampled waveform values used in Fig. 6 are listed in Table 3. They are included so that the pulse locations quoted in the main text can be checked directly against the manuscript bundle.

**Table 3**: Sampled numerical waveform values $\Psi(t, r_*^{\rm obs})$ for the reference characteristic evolution at spacing $\Delta = 0.1M$.

| $t/M$ | $\Psi(t, r_*^{\rm obs})$ |
|---|---|
| 55.0 | -0.03831349 |
| 57.5 | -0.12682880 |
| 60.0 | -0.25683545 |
| 62.5 | -0.13071789 |
| 65.0 | 0.29475398 |
| 67.5 | 0.58047860 |
| 70.0 | 0.37281474 |
| 72.5 | 0.09090636 |
| 75.0 | -0.03160239 |
| 77.5 | -0.07703496 |
| 80.0 | -0.08202446 |
| 82.5 | -0.06939816 |
| 85.0 | -0.05126766 |
| 87.5 | -0.03444444 |
| 90.0 | -0.02094439 |
| 92.5 | -0.01119684 |
| 95.0 | -0.00574478 |
| 97.5 | -0.00389469 |
| 100.0 | -0.00370878 |
| 102.5 | -0.00477746 |
| 105.0 | -0.00563580 |